International Journal of Hydrogen Energy 84 (2024) 793–802

Contents lists available at ScienceDirect

International Journal of Hydrogen Energy

journal homepage: www.elsevier.com/locate/he

Investigating bubble-induced overpotential, current non-uniformity, and bubble distribution in flow-based water electrolyzers: A numerical study

Pooria Hadikhani

Institute of Applied Materials-Electrochemical Technologies (IAM-ET), Karlsruhe Institute of Technology (KIT), Karlsruhe, Germany

ARTICLE INFO

Handling Editor: Dr C O Colpan

Keywords:
Hydrogen
Bubble nucleation
Flow-based electrolzyer
Water electrolysis
Bubble overpotential

ABSTRACT

The transition towards a sustainable energy landscape necessitates efficient and scalable technologies for renewable energy storage. Water electrolysis, a process that converts electrical energy into chemical energy stored in hydrogen, holds immense potential for integration with intermittent renewable sources. However, the performance and efficiency of water electrolyzers are impeded by the complex multiphase flow dynamics involving bubble nucleation, growth, and transport within the electrochemical cell. This study employs state-of-the-art three-dimensional multiphase flow simulations to unravel the intricate interplay between bubbles and the electrochemical processes in a parallel-electrodes flow-based electrolyzer (PE-FBE). By accurately capturing bubble-electrolyte interfaces, the simulations quantify the detrimental effects of bubbles on overpotentials, current density distribution, and bubble distribution. Crucially, the impact of critical parameters, including flow rate, bubble nucleation size, surfactant addition, and applied current, on these performance metrics is systematically investigated. The findings reveal strategies to mitigate bubble-induced losses, enhance current uniformity, and improve hydrogen purity, paving the way for optimized electrolyzer designs and efficient renewable energy storage.

1. Introduction

The use of renewable energy is increasing due to the growing demand for energy and efforts to reduce dependence on fossil fuels [1]. The intermittency of renewable energy sources poses challenges to their integration into the power grid and uninterrupted supply of energy [2]. Consequently, energy storage needs to be integrated into renewable energy power plants in order to meet the power demand from the grid [3]. Energy storage in the form of hydrogen can provide the optimal energy storage method due to its high energy density [4]. Furthermore, hydrogen can be utilized for large-scale energy transport, long-term energy storage, and responding quickly to variable energy demand [5–7]. The electricity from renewable resources can be applied to water electrolyzers to split water molecules into hydrogen and oxygen [8]. The energy storage process remains free from greenhouse gas emissions by utilizing water electrolysis for hydrogen production and energy storage [9]. Improving the efficiency of water electrolyzers will lead to lower operational costs and enable widespread adoption for hydrogen production and energy storage [10]. Understanding the fundamental processes inside water electrolyzers provides insights for improving the design of these devices, leading to more efficient and cost-effective hydrogen production.

Water electrolyzers are classified into high-temperature and low-temperature electrolyzers [11]. High-temperature electrolyzers include solid oxide electrolyzers (SOE), which operate at temperatures higher than 500°C and use water steam for the electrolysis [12]. Low-temperature electrolyzers work at temperatures below 90°C. Alkaline water electrolyzer (AWE), proton exchange membrane (PEM), anion exchange membrane (AEM), and flow-based electrolyzer (FBE) are examples of low-temperature water electrolysis technologies [13,14]. An AWE has two electrodes separated by a diaphragm [15]. The electrodes and the diaphragm are submerged in an alkaline electrolyte. A PEM electrolyzer is made of a polymer membrane with catalysts coated on both sides for hydrogen evolution reaction (HER) and oxygen evolution reaction (OER) [16]. A PEM works in an acidic medium and the membrane allows the migration of protons between the electrodes. An AEM similar to PEM has a membrane with coated catalysts on both sides [17]. However, AEM works in an alkaline medium and hydroxide ions migrate through its membrane. An FBE consists of two electrodes and a liquid electrolyte is flowing between the electrodes [18,19]. The ions migrate between the electrodes through this liquid electrolyte. The electrolyte flow separates the gaseous products from each other [20].

E-mail addresses: Pooria.Hadikhani@kit.edu, p.hadikhani@gmail.com.

https://doi.org/10.1016/j.ijhydene.2024.08.231
Received 20 May 2024; Received in revised form 18 July 2024; Accepted 14 August 2024
Available online 22 August 2024

Therefore, FBEs do not require a membrane or separator.

The low-temperature water electrolyzers work with liquids. At small production rates and high liquid electrolyte flow rates, the gaseous products remain in the dissolved form and no bubble forms on the surface of the electrode [21]. However, the low solubility of hydrogen and oxygen in liquid electrolytes and high production rates lead to the evolution of the products in the form of gas bubbles in water electrolyzers [22]. The bubble evolution consists of three main stages: nucleation, growth, and detachment [23]. Nucleation begins when the concentration of dissolved gas near the electrode surface surpasses saturation, resulting in bubble formation at specific locations [24]. Growth occurs as these bubbles expand due to the continuous influx of dissolved gas from the surrounding liquid [25]. Detachment occurs when detaching forces, such as the liquid drag force, exceed attaching forces, such as surface tension forces, causing the bubble to break away from the electrode surface [26].

The nucleation and growth of bubbles on the surface of the electrode has two opposing effects. On the one hand, the nucleated bubbles on the surface impedes reaction regions and creates a non-uniform current density on the surface of the catalyst [27,28]. On the other hand, the nucleated bubbles reduce the concentration of dissolved gaseous products at the surface of the electrode leading to improved gas evolution reaction [29]. The dynamics of bubble formation and growth are significantly influenced by operational parameters. The bubble growth rate increases by increasing the current density or reducing the flow rate [25,30]. Once the bubbles reach a critical size, they detach from the electrode surface and flow with the electrolyte [31]. The detachment radius of the bubble depends on the surface tension and the drag force from the liquid flow [32]. Furthermore, the geometry and size of the flow channels affect the bubble detachment size [33]. To mitigate the negative effects of bubble formation on the electrode while maximizing its benefits, it is crucial to increase the number of nucleation sites on the electrode surface and promote the detachment of bubbles at smaller sizes [34,35]. This approach can help reduce non-uniformity in current density across the electrode surface while simultaneously decreasing the concentration of dissolved gaseous products [23].

After detachment, the bubbles enter the flow channels and are transported by the flowing liquid electrolyte. During their flow, bubbles can coalesce with other bubbles, forming larger bubbles [36]. The liquid electrolyte properties, liquid velocity, and gas production rate affect the flow of the bubbles and the frequency of bubble coalescence. Considering these parameters, various flow regimes from bubbly flow to slug flow can appear in water electrolyzers [37]. These flow regimes are crucial as they influence the efficiency of mass transfer and the overall energy consumption during the electrolysis process [38]. The presence of bubbles in the electrolyte increases the resistance for ionic transport within liquid electrolytes [39]. This phenomenon leads to the increase of overpotentials [40]. However, the flow of smaller bubbles can reduce these negative effects. Specifically, the presence of smaller bubbles in the electrolyzer leads to the reduction of ohmic overpotentials as it minimizes the impact on ion conduction [41].

Beyond bubbles' impact on overpotentials, the bubbles affect the liquid flow rate inside the electrolyzers, impose higher pressure drops, and induce gas crossover [18]. To reduce the gas crossover and pressure drop related to bubble flow, the size of bubbles should be minimized [36]. This can be achieved by accelerating bubble detachment from the electrode and reducing bubble coalescence frequency. Structuring the electrode surface and increasing the liquid electrolyte flow rate accelerates bubble detachment [42]. The bubble coalescence frequency can be reduced by increasing the flow rate or completely prevented by adding surfactant to the liquid electrolyte [36]. The cell design, operating current density, flow rate, and type of electrolyte affect the bubble growth, detachment, and flow in the electrolyzer and consequently the overpotentials, pressure drop, and gas crossover due to bubbles [26,43,44].

These effects are more pronounced in FBEs as the bubbles flow in the channels in the absence of a separator or a membrane [14]. In this study, we investigate the flow of bubbles in a parallel electrodes flow-based electrolyzer (PE-FBE) [45]. PE-FBE consists of two parallel electrodes acting as the anode and cathode. The electrolyte is flowing between the electrodes. The bubble generation and flow are happening in the inter-electrode area. The flow carries two streams of hydrogen and oxygen bubbles to the end of the electrodes, where bubbles are guided to two separate channels. We quantify the overpotentials caused by bubble nucleation and flow in this electrolyzer. The bubble nucleation size, bubble coalescence, electrolyte flow rate, addition of a surfactant, and applied current are investigated for this quantification. These investigations provide detailed information on the overpotential due to bubbles, the bubble distribution, and the current distribution at the electrode. Three-dimensional multiphase flow simulations are carried out, numerically capturing the interface between the bubbles and the liquid electrolyte, which enables a detailed understanding of the bubble dynamics. The findings derived from these simulations can inform design optimizations [46,47] and enhance the efficiency of electrochemical hydrogen production in water electrolyzers. The bubble generation in this geometry is similar to that in AWE and PEM electrolyzers. Therefore, the outcomes can be extended to other electrolyzers.

2. Methods

To investigate the effect of bubble flow on the performance of FBEs, three-dimensional numerical simulations are conducted using the Aphros multiphase flow solver [48]. Aphros is a versatile tool that has been extensively used to numerically simulate various physical fluid dynamic problems and has been validated against experimental data [49,50]. It simulates bubble generation, bubble-bubble interactions, and coalescence, which are parameters influencing the overpotentials. The incompressible Navier-Stokes equations are solved for the fluid mixture velocity and pressure along with the advection equation to simulate two-component flows.

$$\nabla.\mathbf{u} = 0$$
$$\rho\left(\frac{\partial \mathbf{u}}{\partial t} + (\mathbf{u}.\nabla)\mathbf{u}\right) = -\nabla p + \nabla.\mu\left(\nabla\mathbf{u} + \nabla\mathbf{u}^{T}\right) + \mathbf{f}_{\sigma} \quad \text{Equation 1}$$

and

$$\frac{\partial \alpha}{\partial t} + (\mathbf{u}.\nabla)\alpha = 0 \quad \text{Equation 2}$$

where $\mathbf{u}$, ρ, μ, p, and α are the velocity field of the fluid, mixture density, mixture viscosity, pressure, and gas volume fraction, respectively. The mixture density is given by $\rho = (1-\alpha)\rho_l + \alpha\rho_g$, and the mixture viscosity is defined as $\mu = (1-\alpha)\mu_l + \alpha\mu_g$. The subscripts of l and g denote liquid and gas phases, respectively. $\mathbf{f}_{\sigma} = \sigma\kappa\nabla\alpha$ is the surface tension force, where σ and κ are the surface tension coefficient and the surface curvature at the interface between gas and liquid, respectively. The incompressible Navier-Stokes equations (Equation (1)) are discretized using the second-order projection method [51] and solved using finite volume method. The piecewise linear interface calculation (PLIC) method is used to solve the advection equation (Equation (2)). PLIC reconstructs the interface in each cell containing multiple fluid phases as a plane using the volume fractions. This reconstruction involves calculating interface normal and plane constants. The interface normals are estimated using the volume fractions through the mixed Youngs-centered scheme [52]. The plane constants are calculated using the normals and the volume fractions [53]. The plane splits the cell to match the volume fraction of the phases. The reconstructed interfaces are moved according to the velocity field during the advection.

The steady-state conservation of charge is solved providing the current density distribution and overpotential due to bubbles and ohmic resistance between electrodes. The governing equation for the steady-state conservation of charge is given by:

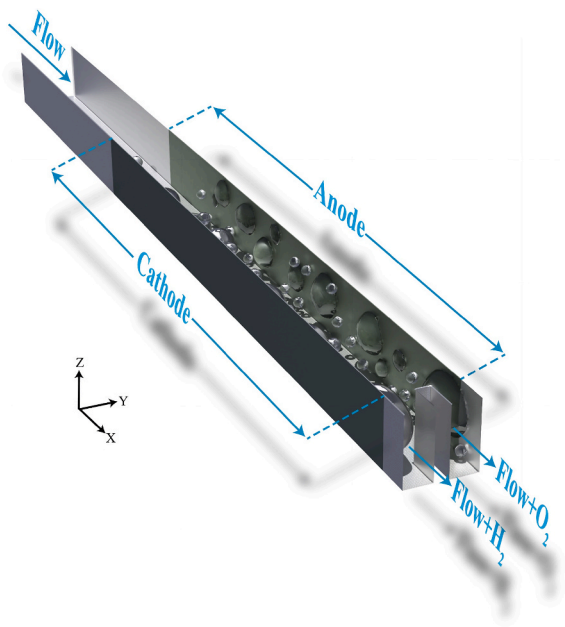

Fig. 1. Simulation snapshot of bubbles' flow in a parallel-electrodes flow-based electrolyzer (PE-FBE) with annotated boundary conditions.

$$\nabla.\mathbf{J} = 0 \qquad \text{Equation 3}$$

where **J** is the current density vector. Ohm's law relates the current density **J** to the electric field **E** and the resistivity ρ_e of the medium:

$$\mathbf{J} = \frac{1}{\rho_e}\mathbf{E} \qquad \text{Equation 4}$$

The electric field **E** can be expressed in terms of the gradient of the electrical potential ϕ.

$$\mathbf{E} = -\nabla\phi \qquad \text{Equation 5}$$

Substituting Equation (4) and Equation (5) in Equation (3) leads to:

$$\nabla.\left(\frac{1}{\rho_e}\nabla\phi\right) = 0 \qquad \text{Equation 6}$$

The resistivity ρ_e between electrodes is changing due to the presence of bubbles, which act as insulating obstacles and alter the effective conductivity of the electrolyte solution. Equation (6) is solved using a second-order finite volume method on a structured grid. Gradients at cell faces are approximated using central differences. Face values are calculated through linear interpolation of adjacent cell centers. The resulting linear system is solved with the conjugate gradient method. The charge conservation solver is validated in section 1 of supplementary information (SI).

Fig. 1 shows a simulation snapshot depicting the flow of bubbles in a PE-FBE, along with the annotated boundary conditions. The electrolyzer geometry is based on the previous PE-FBE experimental study [45], with an interelectrode distance of 1 mm, electrode height of 1 mm, and electrode length of 10 mm. The electrolyte is 0.5 M sulfuric acid with an ionic resistivity of 0.0385 Ohm.m [54]. The simulations are carried out at currents (I) ranging from 30 to 60 mA and flow rates from 300 ml/min to 1200 ml/min. The three-dimensional computational domain dimensions are 16 mm × 1 mm × 1 mm, with all dimensions and variables non-dimensionalized in the simulations. A uniform cubic grid is employed, consisting of 512 × 32 × 32 grid points. Each simulation is executed on 256 cores for a duration of three days.

Bubble coalescence plays a crucial role in determining the bubble size distribution and significantly impacts the electrochemical performance of the system. When bubbles coalesce, they form larger bubbles, which can alter the gas volume fraction distribution, affect the effective electrolyte conductivity, and influence the local current density distribution, and gas bubble movement [55,56]. In the simulations, bubble coalescence is explicitly allowed and modeled. The Aphros multiphase flow solver is capable of simulating bubble-bubble interactions, including coalescence events. This leads to capturing the dynamic evolution of bubble sizes and their subsequent effects on the electrochemical processes.

On the other hand, the presence of surfactants in the electrolyte can significantly alter this behavior by preventing bubble coalescence, leading to a higher number of smaller bubbles and potentially different flow patterns in the electrolyzer. The effect of the addition of surfactant to the electrolyte is studied numerically using the multilayer volume of fluid method (Multi-VOF) feature of Aphros [48]. Multi-VOF is capable of simulating flows with bubbles without allowing them to coalesce. This feature is equivalent to the introduction of surfactants to the liquid electrolyte, which prevents bubble coalescence.

It is important to note that while this study focuses on the effects of surfactants on bubble coalescence, surfactants can potentially influence other aspects of the electrolysis process as well. These include possible effects on electrolyte conductivity and electrode reactions. However, the impact on conductivity is typically minimal at the low surfactant concentrations used to prevent bubble coalescence. For instance, previous experimental studies using Triton X-100 at a concentration of 15×10^{-3} M showed no significant effect on electrolyte conductivity [36]. The influence of surfactants on electrode reactions can vary depending on the specific surfactant used. Some surfactants, such as Triton X-100, may adsorb on the electrode surface, potentially hindering the access of reacting species to the electrode and increasing overpotential [57,58]. In contrast, other surfactants like Heptadecafluorooctancesulfonic acid potassium (PFOS) have been observed to improve reaction kinetics by decreasing hydrogen dissolution in the electrolyte, thereby reducing overpotentials [59]. While the current model does not explicitly account for these electrochemical effects of surfactants, it provides a framework that can be extended to include such considerations by modifying the electrolyte resistivity and catalytic activity. Triton X-100 and PFOS effectively prevent bubble coalescence, and the multi-VOF method used in the numerical simulations can accurately reproduce this behavior.

In the numerical simulations, the inlet and outlet boundary conditions are velocity inlet and pressure outlet, respectively. For the electrodes, the anode has a constant current boundary condition, the cathode has a zero potential boundary condition, and the remaining boundaries are set as insulating boundary conditions. The bubble nucleation occurs in the vicinity of electrodes.

For bubble nucleation, two 2-dimensional regions at the anode and cathode are defined. These regions determine where the bubbles can nucleate. The rate of bubble nucleation is directly proportional to the applied current. In the numerical simulations, the bubble nucleation radii for hydrogen and oxygen bubbles are prescribed as constant values throughout the simulation. The frequency of bubble nucleation is determined based on the applied current and the considered bubble nucleation radius. When the time for the bubble nucleation arrives, the nucleation region is discretized into a grid with spacing equal to half of the bubble nucleation radius. Each grid point is a potential location for bubble nucleation, with the grid point serving as the center of the bubble. For a bubble to nucleate at a grid point, it must be ensured that there are no existing bubbles too close to that point. To enforce this, an offset variable η equal to 1.4 is defined, and the following condition is checked:

> If the minimum distance between a grid point and the center of any existing bubble is smaller than $(r_n.\eta + r_b)$, then that grid point is removed from the list of potential nucleation points. In this condition, r_n is the bubble nucleation radius and r_b is the radius of an existing bubble.
>
> Grid points that do not satisfy this condition are removed. Next,

among the remaining grid points, the points for bubble nucleation are chosen using a uniform random function. If no grid points are available for bubble nucleation, the nucleation radius is divided by $\sqrt[3]{2}$, and the number of bubbles to be nucleated is doubled. By doing this, the total volume of nucleated bubbles remains the same. This process of grid generation and assignment of nucleation points is repeated until bubbles can be successfully nucleated. It should be noted that the grid is two-dimensional and only determines the position of bubbles in a plane parallel to the electrode. The distance from the center of the nucleated bubbles to the electrodes is $r_n.\eta$. In all simulations conducted for this study, sufficient space is consistently available on the electrode surface for bubble nucleation.

The generated hydrogen bubble volume is set to be twice the value of the generated oxygen bubble volume in order to maintain the 2:1 stoichiometric ratio of hydrogen and oxygen production during water electrolysis. The hydrogen bubble nucleation radius ranges from 100 to 200 μm. This range of hydrogen bubble nucleation radius is determined through analysis of visual data presented in Ref. [45]. When the predetermined time for bubble nucleation is reached, the positions for new bubbles are determined using the described method for the bubble nucleation. Afterward, the advection solver is provided with the list of the new bubbles. This solver modifies the volume fraction field to convert from liquid to gas phase at the specified nucleation sites.

This research investigates high current densities. At such high current densities, the ratio of dissolved products to gaseous products in the bubble form is negligible. Consequently, this study assumes that all the products are generated as bubbles. The bubbles can reside on the surface of the electrodes resulting in the reduction of the active surface area available for the electrochemical reaction. To account for this, the active surface area is calculated at each time step based on the bubble coverage, and the current density is adjusted accordingly to keep the electrical current constant.

2.1. Effect of bubbles on the overpotentials

The total electrical potential (E_{cell}) required to operate an electrochemical reaction is the sum of the thermodynamics equilibrium potential (E_0), the activation overpotential at the cathode ($\eta_{cathode}$) and the anode (η_{anode}), the ohmic resistance between electrodes (η_{ohmic}), and the diffusion overpotential due to the development of concentration gradient at the surface of the electrode ($\eta_{diffusion}$).

$$E_{cell} = E_0 + \eta_{cathode} + \eta_{anode} + \eta_{ohmic} + \eta_{diffusion} \quad \text{Equation 7}$$

The bubble generation in an electrochemical reaction affects all the overpotentials [60,61]. Initially, a bubble nucleates on the surface of the electrode. The presence of this bubble on the surface reduces the available active area for the reaction. This area reduction leads to an increase in the current density and consequently an increase in the activation overpotentials $\eta_{cathode}$ and η_{anode}. Furthermore, bubble nucleation reduces the concentration of dissolved gas in the vicinity of electrodes. This concentration reduction lowers the concentration overpotential. Finally, the nucleation, detachment, and flow of bubbles in PE-FBEs occur in the interelectrode regions. These bubbles block ionic pathways and augment the ohmic resistance between the electrodes. Thus, bubble generation and flow in FBEs increase the ohmic resistance overpotential (η_{ohmic}).

To quantify the effect of bubbles on activation overpotentials, a two-step process is employed. First, the surface coverage of the electrode by bubbles is determined from the numerical simulations. Second, the Tafel equation is used to calculate the activation overpotentials both with and without electrode surface coverage by bubbles. The difference between these values provides the additional activation overpotential due to bubbles. The bubble-induced activation overpotential ($\eta^b_{activation}$) at the electrode is calculated as:

$$\eta^b_{activation} = \beta \log\left(\frac{j}{j_0(1-\theta)}\right) - \beta \log\left(\frac{j}{j_0}\right) \quad \text{Equation 8}$$

where β is the Tafel slope, j is the applied current density, j_0 is the exchange current density, and θ is the fraction of the electrode surface covered by bubbles. For OER in an acidic medium, the Tafel slope is 100 mV dec^{-1} and the exchange current density is 4×10^{-10} A.cm^{-2} [62]. For HER, the Tafel slope is 32 mV dec^{-1} and the exchange current density is 1.3×10^{-3} A.cm^{-2} [40,63]. The bubble-induced activation overpotential at the cathode and anode are calculated using Equation (8) and are denoted by η^b_{HER} and η^b_{OER}, respectively. A similar procedure is employed to calculate the bubble-induced ohmic overpotential. Equation (6) is solved under two conditions: first, with bubbles present in the system ($\eta_{ohmic,with\ bubbles}$), and second, in the absence of bubbles where

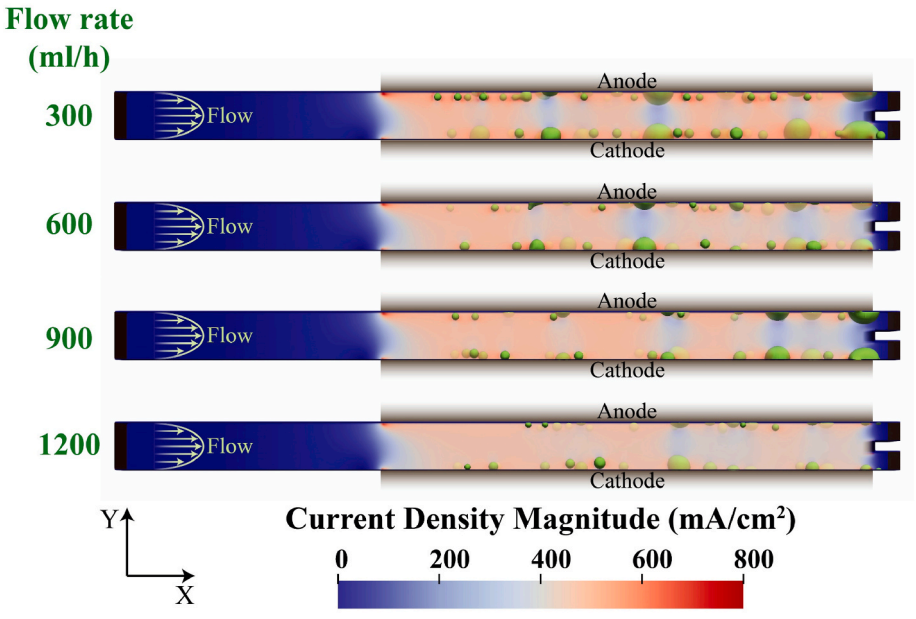

Fig. 2. Bubble generation and flow at flow rates of 300, 600, 900, and 1200 ml/h and constant current of 45 mA. The hydrogen bubble nucleation radius is 101 μm. The image shows a volume contour of the current density magnitude. The volume contour has a semi-transparent opacity level, allowing the bubbles to be visible.

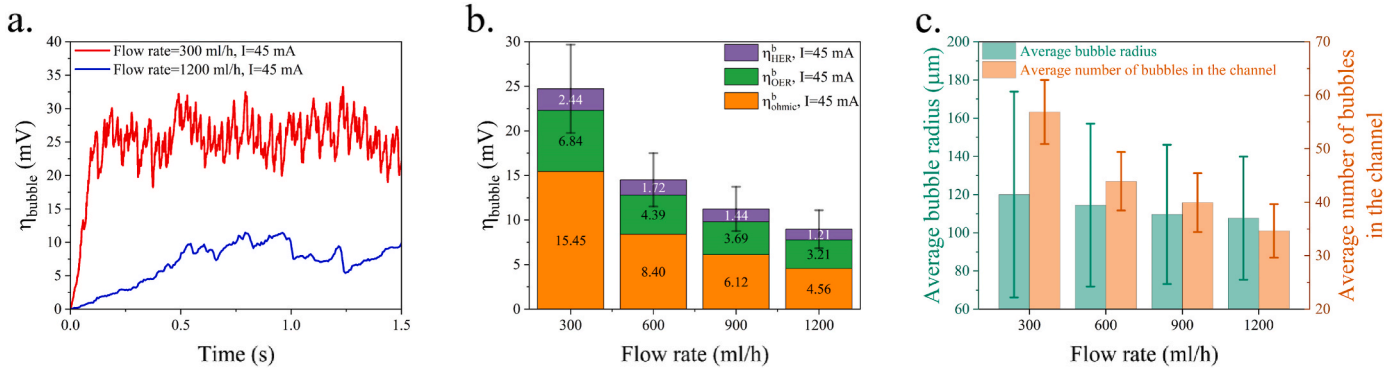

Fig. 3. Bubble behavior and effects on the overpotential in the PE-FBE at different flow rates, 45 mA applied current, 101 μm hydrogen bubble nucleation radius. (a) Evolution of bubble overpotential over time for flow rates of 300 and 1200 ml/h. (b) Steady-state average bubble overpotential (showing HER, OER, and ohmic components) and standard deviation at flow rates of 300, 600, 900, and 1200 ml/h. The standard deviation is for the total bubble overpotential (η_{bubble}). (c) Average bubble radius and number of bubbles in the channel at different flow rates under steady-state conditions.

the interelectrode region is filled only with electrolyte ($\eta_{ohmic,without\ bubbles}$). The bubble-induced ohmic overpotential (η^b_{ohmic}) is then calculated as the difference between these two values:

$$\eta^b_{ohmic} = \eta_{ohmic,with\ bubbles} - \eta_{ohmic,without\ bubbles} \quad \text{Equation 9}$$

This approach isolates the additional ohmic overpotential caused specifically by the presence of bubbles in the system.

Although bubbles affect the concentration overpotential, the significance of this overpotential depends on the flow velocity and the diffusion coefficient of dissolved gases. The Peclet number (Pe) is defined as:

$$Pe = \frac{VL}{D_{dif}} \quad \text{Equation 10}$$

determines the ratio of convective flows to the diffusion. In this equation, V is the velocity of the liquid, L is the interelectrode distance, and D_{dif} is the diffusion coefficient. In the PE-FBE investigated in this study, the Peclet number is larger than 10000 considering the liquid velocity and diffusion coefficients of oxygen, hydrogen, and protons. This large value indicates that the convective flow dominates over diffusion. Therefore, the liquid flow replenishes the reactants and removes dissolved gases efficiently close to the electrodes leading to very small concentration gradient [25]. Consequently, the concentration gradient overpotential is small and the effect of bubbles on this overpotential is neglected.

The accumulative effect of bubbles on the overpotentials is referenced as bubble overpotential (η_{bubble}) in the next section. η_{bubble} represents the difference between overpotentials in the absence and presence of bubbles and is calculated as below:

$$\eta_{bubble} = \eta^b_{ohmic} + \eta^b_{HER} + \eta^b_{OER} \quad \text{Equation 11}$$

3. Results

The bubble distribution inside FBEs, the bubble overpotential, and the current density distribution are strongly dependent on the liquid electrolyte flow, electrolyte properties, bubble nucleation size, and applied current. Quantifying the effect of these parameters on the performance of FBEs leads to the definition of strategies for the reduction of inefficiencies while enhancing the production rate and purity of hydrogen. The following sections provide the numerical results of studying these parameters.

3.1. Flow rate

Fig. 2 shows a snapshot of the numerical simulation of bubbles flowing in the PE-FBE along with the current density magnitude distribution at different flow rates. The applied current and hydrogen bubble nucleation radius are 45 mA and 101 μm, respectively, as obtained from experimental data reported in Ref. [45]. The bubble nucleation size is measured from the experimental images in Ref. [45]. The experiments were conducted under the same geometric configuration and operating conditions as those used in the simulations. The evolution of the bubble overpotential over time is shown for two flow rates of 300 ml/h and 1200 ml/h in Fig. 3a. The contribution of bubble-induced ohmic and activation overpotentials to the bubble overpotential at flow rates of 300 ml/h and 1200 ml/h is shown in Figure SI.2. The bubble overpotential initially grows when the electrochemical reaction and bubble generation start. Eventually, the fluctuations in the bubble overpotential stabilize when the bubble generation rate becomes equal to the bubble removal rate from the channel facilitated by the electrolyte flow. The images shown in Fig. 2 are taken when the bubble overpotential reaches this steady-state condition.

Fig. 3b indicates the average and standard deviation values of bubble overpotential at four different flow rates at the steady-state condition. Furthermore, bubble-induced ohmic and activation overpotentials are depicted in this figure. The major part of the bubble overpotential comes from the ohmic resistance increase due to the presence of bubbles, reflected in the bubble-induced ohmic overpotential. Moreover, the bubble-induced activation overpotential at the anode side is larger than at the cathode side since the oxygen evolution reaction (OER) is more energy-intensive and experiences greater losses compared to the hydrogen evolution reaction (HER). The bubble overpotential is decreasing by increasing the flow rate as the higher flow rate removes the bubbles faster from the channel. Furthermore, the number of bubbles inside the channel and bubbles' radii are smaller at higher flow rates due to the lower residency time of bubbles inside the channel and a reduced rate of bubble coalescence as shown in Fig. 3c. The decrease in the bubble size and number with increasing flow rate aligns with experimental observations reported in the literature [64].

The ohmic resistance overpotential in the absence of bubbles in this FBE channel is 164 mV. The bubble overpotential is the additional overpotential caused by the presence of bubbles. Consequently, at the working current of 45 mA, the bubble-induced ohmic overpotential is changing from 8.63% of total ohmic overpotential (ohmic overpotential plus bubble-induced ohmic overpotential) at the flow rate of 300 ml/h to 2.71% of total ohmic overpotential. While operating at higher flow rates demands greater pumping power, the resulting reduction in bubble overpotential losses outweighs this increased pumping power requirement. Therefore, operating at higher flow rates improves the overall system efficiency by mitigating the detrimental effects of bubbles on the ohmic resistance. The calculation of power required for flowing the liquid electrolyte is described in SI section 3. Although the contribution

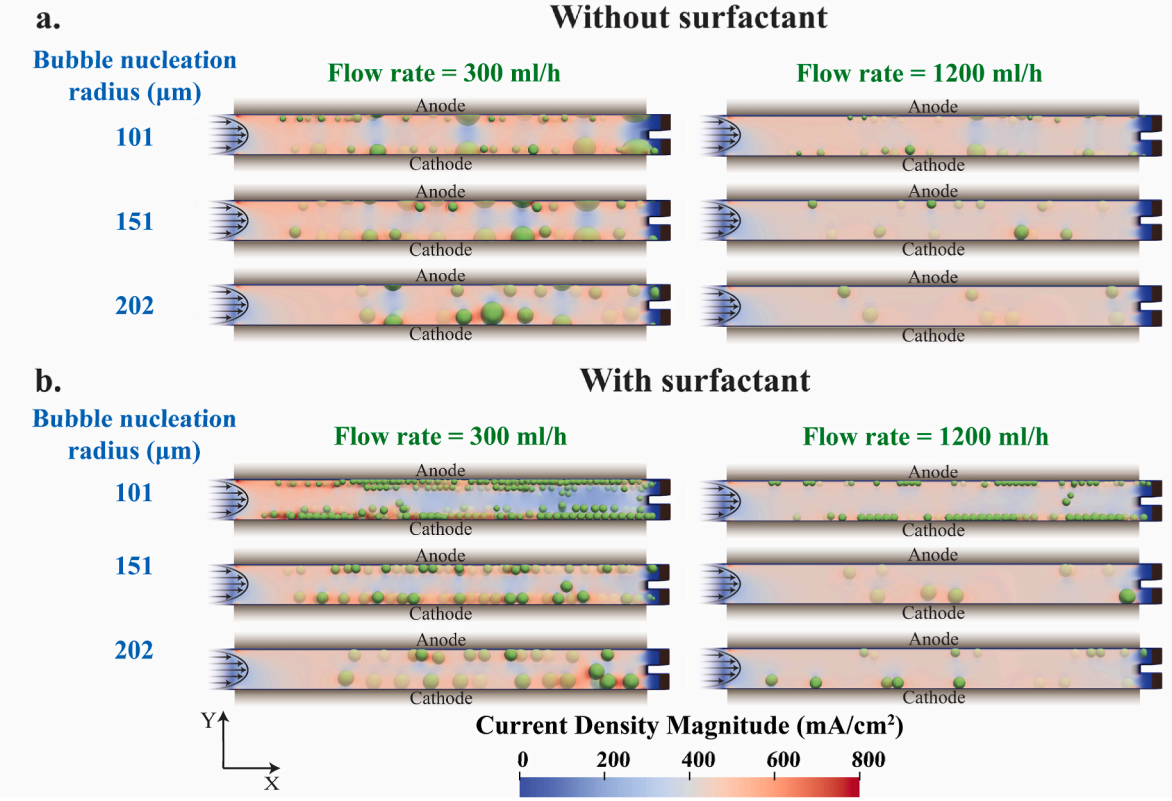

Fig. 4. Bubble generation and flow at flow rates of 300 ml/min and 1200 ml/min showing the effect of bubble nucleation sizes (101, 151, 202 μm) in an electrolyte (a) without surfactant and (b) with surfactant. The images show the volume contours of the current density magnitude. Volume contours have a semi-transparent opacity level, allowing the bubbles to be visible.

of the electrolyte pumping power to the total input power is relatively small, high flow rates can significantly complicate the design of electrolyzer stacks, where a substantial flow rate would be required to supply the liquid electrolyte to all cells within the stack. Moreover, the electrolyte flow rate cannot exceed a certain threshold value to ensure laminar flow conditions.

3.2. *Bubble nucleation size and surfactant*

The bubble size affects the bubble overpotential due to the electrode surface coverage and ionic pathway blockage in the interelectrode region by bubbles. Furthermore, the amount of gas cross-over is related to the bubble size, as it determines the bubble's lateral position in the channel [44]. Two main factors determine the bubble size: nucleation size and coalescence [65]. The nucleation size of the bubble can be controlled by changing the surface properties of the electrode, including surface roughness and contact angle [66]. The coalescence of the bubbles can be controlled by adding surfactants to the liquid electrolyte [36]. The surfactant molecules migrate to the interface between the gas and liquid phase, preventing bubble coalescence [67]. In this section, numerical simulations are carried out with three different hydrogen bubble nucleation radii of 101 μm, 151 μm, and 202 μm to simulate the effect of changing electrode surface properties. Moreover, the same simulations are performed for the case where bubble coalescence is prohibited to simulate the effect of surfactant addition to the electrolyte. Fig. 4a and b show snapshots of bubbles flowing at two different flow rates of 300 ml/h and 1200 ml/h for the electrolytes without and with surfactant.

Fig. 5a shows the bubble overpotential of the simulated cases versus the bubble nucleation size. Within the range of bubble nucleation sizes investigated in this study, a larger bubble nucleation size results in a lower bubble overpotential. This trend can be explained by the bubble size distribution in the channel at different nucleation sizes, as depicted in Figure SI.2, and the bubble volume fraction inside the channel, shown in Fig. 5b. In Fig. 5b, the bubble volume fraction is the ratio of the volume occupied by the hydrogen and oxygen bubbles to the total available volume between the electrodes. A larger bubble volume fraction results in higher overpotentials as it increases the ohmic resistance between electrodes. On the other hand, a large bubble blocks fewer ionic pathways between electrodes compared to multiple small bubbles that have the same total volume. Additionally, larger bubbles are flowing faster than smaller bubbles and leave the channel earlier. Based on the facts presented, a large bubble nucleation size is advantageous as it results in larger bubbles flowing in the channel and a smaller overall bubble volume fraction, both of which contribute to a lower bubble overpotential.

At a small flow rate of 300 ml/h, the electrolyte with a surfactant has a higher bubble overpotential compared to the electrolyte without the surfactant as shown in Fig. 5d and Fig. 5a. Figure SI4 shows that the electrolyte with surfactant prevents bubble coalescence. Therefore, the number of bubbles increases in the electrolyte with surfactant compared to the surfactant-free electrolyte resulting in more area coverage between electrodes by the bubbles and higher ohmic resistance. Furthermore, bubbles have a smaller size in an electrolyte with surfactant compared to the electrolyte without surfactant. These small bubbles stay closer to the electrode surface and have a smaller velocity compared to larger bubbles leading to a higher bubble volume fraction in the electrolyte with surfactant in comparison with the electrolyte without surfactant at 300 ml/h flow rate as shown in Fig. 5e. At the flow rate of 1200 ml/h, the bubble flow pattern in both electrolytes is similar since the bubble coalescence is infrequent in the electrolyte without surfactant. Consequently, the bubble overpotential is almost the same for both electrolytes at this flow rate.

Although the addition of surfactant at lower flow rates increases the

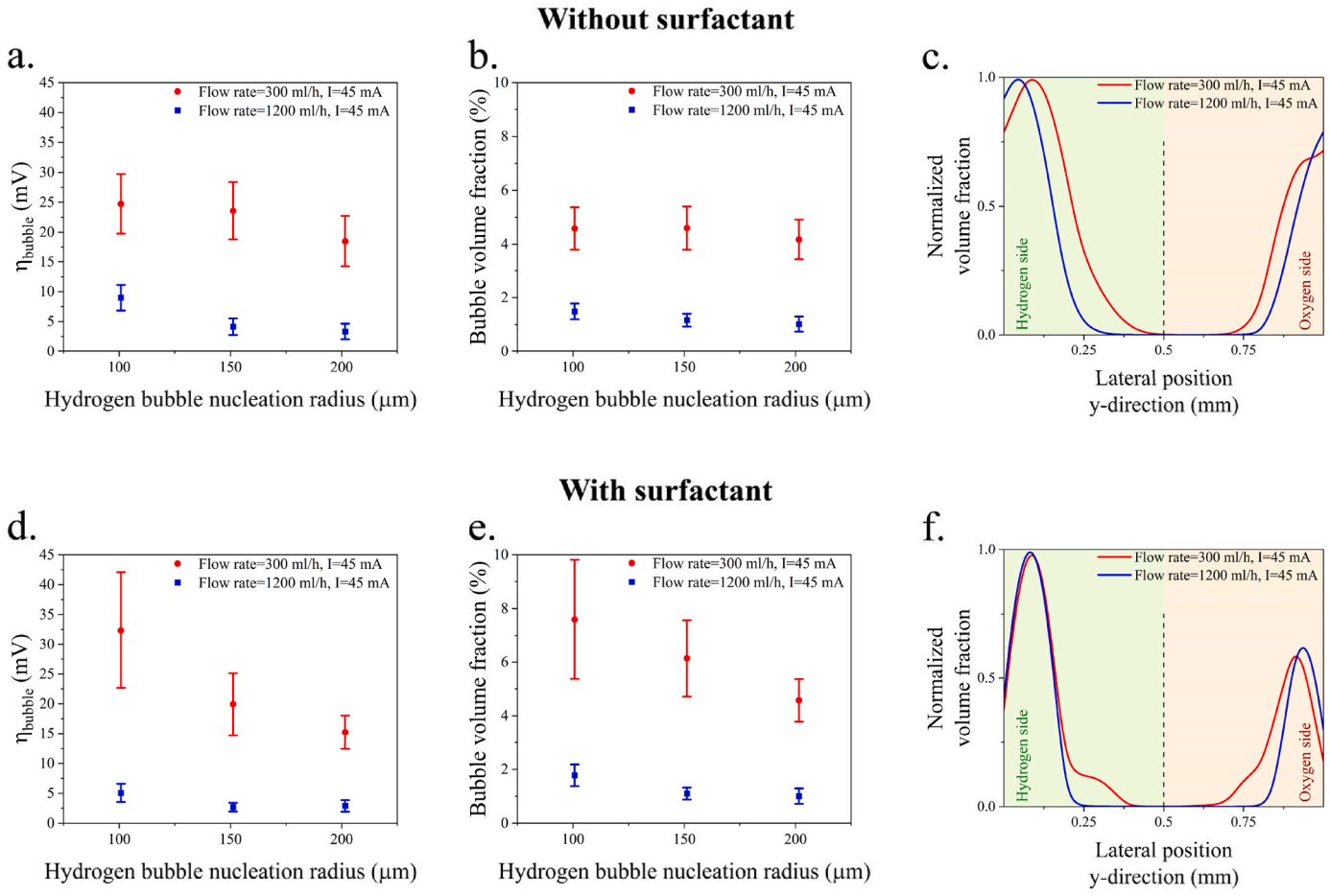

Fig. 5. Effect of bubble nucleation radius and surfactant on (a) and (d) bubble overpotential, (b) and (e) bubble volume fraction, and (c) and (f) lateral bubble distribution. The hydrogen bubble nucleation radius in (c) and (f) is 101 μm.

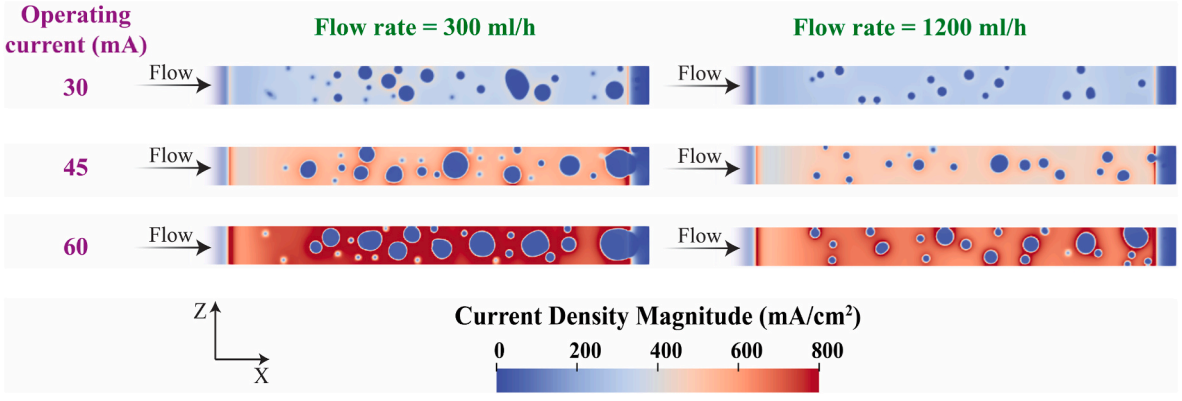

Fig. 6. Current density magnitude distribution on the cathode surface at operating currents of 30 mA, 45 mA, and 60 mA for flow rates of 300 ml/h and 1200 ml/h, showing the effect of bubble coverage on the current non-uniformity. The hydrogen bubble nucleation radius is 101 μm in the simulations.

bubble overpotential, it improves the purity of hydrogen production. Fig. 5c and Fig. 5f show the bubble distribution between electrodes. As described in the previous paragraph, bubbles stay closer to the electrodes and further from the middle in the electrolyte with surfactant. Consequently, at the flow rate of 300 ml/h, the bubbles in the electrolyte with surfactant are distributed farther away from the centerline compared to the bubbles in the electrolyte without surfactant. Thus, the addition of surfactant reduces the gas cross-over. It should be noted that the bubble distribution between electrodes is similar in both electrolytes with and without surfactant at the flow rate of 1200 ml/h due to the similar bubble flow pattern.

3.3. Applied current

The current uniformity at the surface of the electrode determines the efficiency of electrolysis and the lifetime of the electrode [68]. Bubbles growing on the surface of the electrode or flowing close to it prevent electrochemical reactions in that region. In this case, the current density on the other regions of the electrode increases when the electrolyzer is operating at constant current for steady hydrogen production. The

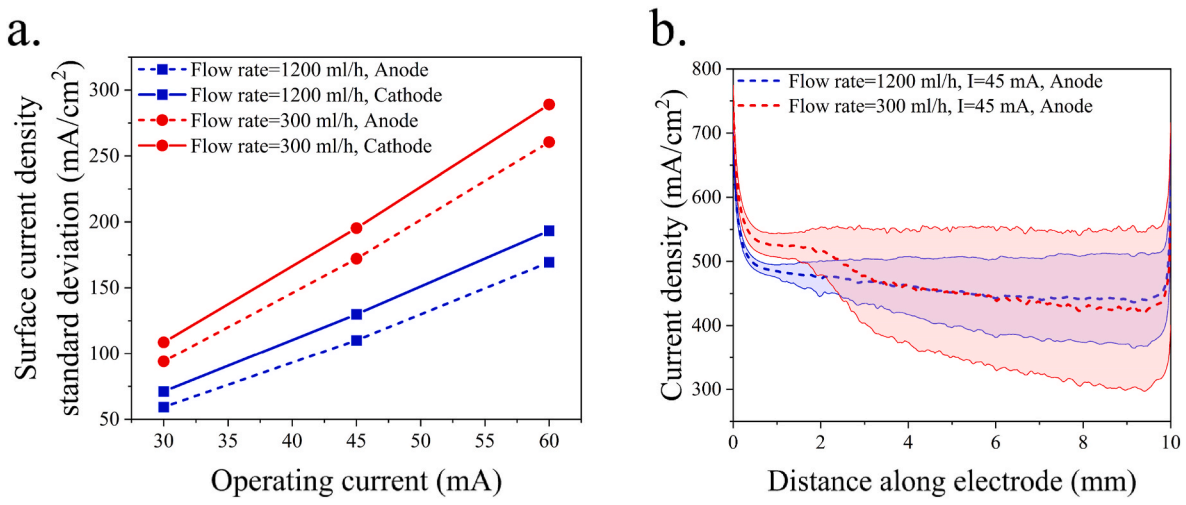

Fig. 7. (a) Variation of current density on the cathode and anode surfaces at different operating currents and flow rates. (b) Increase in current density variation across the electrode surface from inlet to outlet due to progressive bubble accumulation along the flow direction, with the average current density decreasing along the electrode. The hydrogen bubble nucleation radius is 101 μm in the simulations.

reduced area of the reaction leads to an increase in the activation overpotential due to increased current density.

Fig. 6 shows the current density magnitude distribution at the surface of the cathode at three operating currents of 30, 45, and 60 mA and two flow rates of 300 and 1200 ml/h. This figure depicts current density magnitude sudden changes in the vicinity of bubble edges which can deteriorate the catalyst and reduce its lifetime. The current density is higher at the edges of bubbles compared to the regions on the electrode surface unaffected by bubbles. This is due to the distortion of the electric field lines caused by the presence of the non-conducting gas bubbles, leading to a higher current concentration at the bubble-electrolyte interface. Fig. 7a shows the standard deviation of the current density on the surface of the cathode and anode. The current density has a larger variation at the cathode surface than the anode surface because of higher gas generation on the cathode side. Furthermore, the variation of current density decreases when the flow rate increases and/or the applied current decreases. This is due to lower surface coverage by the bubbles at higher flow rates and/or lower currents.

The presence of gas bubbles between the electrodes in the PE-FBE accumulates progressively along the flow direction. This is because newly generated bubbles from the electrochemical reactions, as well as those carried from upstream, contribute to an increasing bubble population towards the end of the electrode. As a result, the average current density decreases from the inlet to the outlet due to higher overall electrode surface coverage by bubbles, as shown in Fig. 7b. Furthermore, the variation and non-uniformity in current density across the electrode surface increases progressively along the flow direction. At higher flow rates, the decrease in current density and the increase in variation are less pronounced, as the volume fraction of bubbles in the channel becomes smaller, and the faster flow removes bubbles more effectively from the channel.

4. Conclusion

The present work leverages state-of-the-art numerical simulations to provide unprecedented insights into the intricate dynamics of bubble nucleation and transport within water electrolyzers. By accurately capturing the bubble-electrolyte interfaces, the simulations elucidate the detrimental effects of bubbles on critical performance metrics, including overpotentials, current density distribution, and bubble distribution. Crucially, the systematic investigation of key parameters, such as flow rate, bubble nucleation size, surfactant addition, and applied current, unveils strategies to mitigate bubble-induced losses, enhance current uniformity, and improve hydrogen purity.

The findings of this study have far-reaching implications beyond the specific PE-FBE geometry investigated. The fundamental understanding gained can be applied to all electrochemical technologies involving bubble nucleation, enabling a better comprehension of their performance limitations and optimization pathways. Moreover, the developed numerical platform can be integrated with optimization tools and algorithms, facilitating the design and enhancement of electrolyzers and other electrochemical devices. As the global transition towards sustainable energy systems accelerates, the insights and methodologies presented herein hold the promise of enabling more efficient and cost-effective renewable energy storage through optimized water electrolysis technologies, ultimately contributing to the realization of a carbon-neutral energy landscape.

Data availability

The simulation data and data used for the figures are available at https://doi.org/10.5281/zenodo.11147251. The setup of the numerical simulations is available at https://doi.org/10.5281/zenodo.11147103.

CRediT authorship contribution statement

Pooria Hadikhani: Writing – review & editing, Writing – original draft, Visualization, Validation, Software, Resources, Project administration, Methodology, Investigation, Funding acquisition, Formal analysis, Data curation, Conceptualization.

Declaration of competing interest

The authors declare that they have no known competing financial interests or personal relationships that could have appeared to influence the work reported in this paper.

Acknowledgments

This work is supported by “Ministerium Für Wissenschaft Forschung Und Kunst of Baden Württemberg” and “Bundesministerium für bildung und Forschung of Germany”. This work was performed on the HoreKa supercomputer funded by the Ministry of Science, Research and the Arts Baden-Württemberg and by the Federal Ministry of Education and Research. The author acknowledges support from the state of Baden-Württemberg through bwHPC.

Appendix A. Supplementary data

Supplementary data to this article can be found online at https://doi.org/10.1016/j.ijhydene.2024.08.231.

References

[1] Osman Ahmed I, Chen Lin, Yang Mingyu, Msigwa Goodluck, Farghali Mohamed, Fawzy Samer, Rooney David W, Yap Pow-Seng. Cost, environmental impact, and resilience of renewable energy under a changing climate: a review. Environ Chem Lett 2023;21(2):741–64. https://doi.org/10.1016/j.enconman.2021.114040.

[2] Mlilo Njabulo, Brown Jason, Ahfock Tony. Impact of intermittent renewable energy generation penetration on the power system networks–A review. Technology and Economics of Smart Grids and Sustainable Energy 2021;6(1):25. https://doi.org/10.1007/s40866-021-00123-w.

[3] Alexander J Headley, Copp David A. Energy storage sizing for grid compatibility of intermittent renewable resources: a California case study. Energy 2020;198:117310. https://doi.org/10.1016/j.energy.2020.117310.

[4] Hassan Qusay, Sameen Aws Zuhair, Salman Hayder M, Jaszczur Marek, Al-Jiboory Ali Khudhair. Hydrogen energy future: advancements in storage technologies and implications for sustainability. J Energy Storage 2023;72:108404. https://doi.org/10.1016/j.est.2023.108404.

[5] Itzel Serrano-Arévalo Tania, Tovar-Facio Javier, María Ponce-Ortega José. Optimal incorporation of intermittent renewable energy storage units and green hydrogen production in the electrical sector. Energies 2023;16(6):2609. https://doi.org/10.3390/en16062609.

[6] Semeraro III Michael A. Renewable energy transport via hydrogen pipelines and HVDC transmission lines. Energy Strategy Rev 2021;35:100658. https://doi.org/10.1016/j.esr.2021.100658.

[7] Gabrielli Paolo, Poluzzi Alessandro, Jan Kramer Gert, Spiers Christopher, Mazzotti Marco, Gazzani Matteo. Seasonal energy storage for zero-emissions multi-energy systems via underground hydrogen storage. Renew Sustain Energy Rev 2020;121:109629. https://doi.org/10.1016/j.rser.2019.109629.

[8] Mohammadi Amin, Mehrpooya Mehdi. A comprehensive review on coupling different types of electrolyzer to renewable energy sources. Energy 2018;158:632–55. https://doi.org/10.1016/j.energy.2018.06.073.

[9] Shiva Kumar S, Lim Hankwon. An overview of water electrolysis technologies for green hydrogen production. Energy Rep 2022;8:13793–813. https://doi.org/10.1016/j.egyr.2022.10.127.

[10] Oliveira Alexandra M, Beswick Rebecca R, Yan Yushan. A green hydrogen economy for a renewable energy society. Curr Opinion Chem Eng 2021;33:100701. https://doi.org/10.1016/j.coche.2021.100701.

[11] Rashid MD, Al Mesfer Mohammed K, Hamid Naseem, Danish Mohd. Hydrogen production by water electrolysis: a review of alkaline water electrolysis, PEM water electrolysis and high temperature water electrolysis. Int J Eng Adv Technol 2015.

[12] Laguna-Bercero Miguel A, Wang Yudong, Zhou Xiao-Dong, Zhu Liangzhu. Fundamentals of solid oxide electrolysis cells (SOEC). In: High temperature electrolysis. Springer; 2023. p. 5–34. https://doi.org/10.1007/978-3-031-22508-6_2.

[13] Li Wei, Tian Hanchen, Ma Liang, Wang Yi, Liu Xingbo, Gao Xuefei. Low-temperature water electrolysis: fundamentals, progress, and new strategies. Mater Advan 2022;3(14):5598–644. https://doi.org/10.1039/D2MA00185C.

[14] Pooria Hadikhani, Membrane-less alkaline water electrolyzers: current state of research. https://doi.org/10.1149/osf.io/abpjq.

[15] Sharshir Swellam W, Joseph Abanob, Elsayad Mamoun M, Tareemi Ahmad A, Kandeal AW, Elkadeem Mohamed R. A review of recent advances in alkaline electrolyzer for green hydrogen production: performance improvement and applications. Int J Hydrogen Energy 2023. https://doi.org/10.1016/j.ijhydene.2023.08.107.

[16] Chen Yuhao, Liu Chaofan, Xu Jingcheng, Xia Chengfeng, Wang Ping, Xia Bao Yu, Yan Ya, Wang Xianying. Key components and design strategy for a proton exchange membrane water electrolyzer. Small Struct 2023;4(6):2200130. https://doi.org/10.1002/sstr.202200130.

[17] Zakaria Zulfirdaus, Kartom Kamarudin Siti. A review of alkaline solid polymer membrane in the application of AEM electrolyzer: Materials and characterization. Int J Energy Res 2021;45(13):18337–54. https://doi.org/10.1002/er.6983.

[18] Hadikhani Pooria, Hashemi SMohammad H, Schenk Steven A, Psaltis Demetri. A membrane-less electrolyzer with porous walls for high throughput and pure hydrogen production. Sustain Energy Fuels 2021;5(9):2419–32. https://doi.org/10.1039/D1SE00255D.

[19] Hashemi SMohammad H, Modestino Miguel A, Psaltis Demetri. A membrane-less electrolyzer for hydrogen production across the pH scale. Energy Environ Sci 2015;8(7):2003–9. https://doi.org/10.1039/C5EE00083A.

[20] Daniel V Esposito. Membraneless electrolyzers for low-cost hydrogen production in a renewable energy future. Joule 2017;1(4):651–8. https://doi.org/10.1016/j.joule.2017.07.003.

[21] Lee Jaeseung, Alam Afroz, Park Chungi, Yoon Soobin, Ju Hyunchul. Modeling of gas evolution processes in porous electrodes of zero-gap alkaline water electrolysis cells. Fuel 2022;315:123273. https://doi.org/10.1016/j.fuel.2022.123273.

[22] Battistel Alberto, Dennison Christopher R, Lesch Andreas, Girault Hubert H. Local study on hydrogen and hydrogen gas bubble formation on a platinum electrode. J Phys Chem C 2019;123(17):10849–56. https://doi.org/10.1021/acs.jpcc.8b10920.

[23] Yuan Shu, Zhao Congfan, Cai Xiyang, An Lu, Shen Shuiyun, Yan Xiaohui, Zhang Junliang. Bubble evolution and transport in PEM water electrolysis: mechanism, impact, and management. Prog Energy Combust Sci 2023;96:101075. https://doi.org/10.1016/j.pecs.2023.101075.

[24] Dapkus Kestutis V, Sides Paul J. Nucleation of electrolytically evolved hydrogen at an ideally smooth electrode. J Colloid Interface Sci 1986;111(1):133–51. https://doi.org/10.1016/0021-9797(86)90014-7.

[25] Khalighi Faeze, Deen Niels G, Tang Yali, Vreman Albertus W. Hydrogen bubble growth in alkaline water electrolysis: an immersed boundary simulation study. Chem Eng Sci 2023;267:118280. https://doi.org/10.1016/j.ces.2022.118280.

[26] Taqieddin Amir, Nazari Roya, Rajic Ljiljana, Alshawabkeh Akram. Physicochemical hydrodynamics of gas bubbles in two phase electrochemical systems. J Electrochem Soc 2017;164(13):E448. https://doi.org/10.1149/2.1161713jes.

[27] Angulo Andrea, van der Linde Peter, Gardeniers Han, Modestino Miguel, Rivas David Fernández. Influence of bubbles on the energy conversion efficiency of electrochemical reactors. Joule 2020;4(3):555–79. https://doi.org/10.1016/j.joule.2020.01.005.

[28] Mandin Philippe, Hamburger Jérôme, Bessou Sebastien, Picard Gérard. Modelling and calculation of the current density distribution evolution at vertical gas-evolving electrodes. Electrochim Acta 2005;51(6):1140–56. https://doi.org/10.1016/j.electacta.2005.06.007.

[29] Higuera FJ. A model of the growth of hydrogen bubbles in the electrolysis of water. J Fluid Mech 2021;927:A33. https://doi.org/10.1017/jfm.2021.778.

[30] Li Yifan, Yang Gaoqiang, Yu Shule, Kang Zhenye, Mo Jingke, Han Bo, Talley Derrick A, Zhang Feng-Yuan. In-situ investigation and modeling of electrochemical reactions with simultaneous oxygen and hydrogen microbubble evolutions in water electrolysis. Int J Hydrogen Energy 2019;44(52):28283–93. https://doi.org/10.1016/j.ijhydene.2019.09.044.

[31] Fernandez Damaris, Maurer Paco, Martine Milena, Coey JMD, Möbius Matthias E. Bubble formation at a gas-evolving microelectrode. Langmuir 2014;30(43):13065–74. https://doi.org/10.1021/la500234r.

[32] Nouri-Khorasani Amin, Ojong Emile Tabu, Smolinka Tom, Wilkinson David P. Model of oxygen bubbles and performance impact in the porous transport layer of PEM water electrolysis cells. Int J Hydrogen Energy 2017;42(48):28665–80. https://doi.org/10.1016/j.ijhydene.2017.09.167.

[33] Shepard Thomas G, Lee Jaiho, Yan Bo, Strykowski Paul J. Parameters affecting bubble formation and size distribution from porous media. J Fluid Eng 2016;138(3):031202. https://doi.org/10.1115/1.4031534.

[34] Li Yingjie, Zhang Haichuan, Xu Tianhao, Lu Zhiyi, Wu Xiaochao, Wan Pengbo, Sun Xiaoming, Jiang Lei. Under-water superaerophobic pine-shaped Pt nanoarray electrode for ultrahigh-performance hydrogen evolution. Adv Funct Mater 2015;25(11):1737–44. https://doi.org/10.1002/adfm.201404250.

[35] Li Long, Jiang Wenjun, Zhang Guang, Feng Deqiang, Zhang Ce, Yao Wei, Wang Zhijie. Efficient mesh interface engineering: insights from bubble dynamics in electrocatalysis. ACS Appl Mater Interfaces 2021;13(38):45346–54. https://doi.org/10.1021/acsami.1c07637.

[36] Hadikhani Pooria, Hashemi SMohammad H, Psaltis Demetri. The impact of surfactants on the inertial separation of bubbles in microfluidic electrolyzers. J Electrochem Soc 2020;167(13):134504. https://doi.org/10.1149/1945-7111/abb6ca.

[37] Coskun Avci Arzu, Toklu Ethem. A new analysis of two phase flow on hydrogen production from water electrolysis. Int J Hydrogen Energy 2022;47(11):6986–95. https://doi.org/10.1016/j.ijhydene.2021.03.180.

[38] Aubras Farid, Deseure J, Kadjo J-JA, Dedigama I, Majasan J, Grondin-Perez Brigitte, Chabriat J-P, Brett DJL. Two-dimensional model of low-pressure PEM electrolyser: two-phase flow regime, electrochemical modelling and experimental validation. Int J Hydrogen Energy 2017;42(42):26203–16. https://doi.org/10.1016/j.ijhydene.2017.08.211.

[39] Cao Xuepu, Zhao Ning, Zhang Shirong, Zhou Lilong, Hu Yongqi, Yun Jimmy. Investigation of the hydrogen bubble effect on the overpotential in an alkaline water electrolyzer. Int J Hydrogen Energy 2024;49:47–57. https://doi.org/10.1016/j.ijhydene.2023.06.242.

[40] Pang Xueqi, Davis Jonathan T, Harvey Albert D, V Esposito Daniel. Framework for evaluating the performance limits of membraneless electrolyzers. Energy Environ Sci 2020;13(10):3663–78. https://doi.org/10.1039/D0EE02268C.

[41] Torii Kenjiro, Kodama Manabu, Hirai Shuichiro. Three-dimensional coupling numerical simulation of two-phase flow and electrochemical phenomena in alkaline water electrolysis. Int J Hydrogen Energy 2021;46(71):35088–101. https://doi.org/10.1016/j.ijhydene.2021.08.101.

[42] He Yi, Cui Yifan, Zhao Zhongxi, Chen Yongtang, Shang Wenxu, Tan Peng. Strategies for bubble removal in electrochemical systems. Energy Rev 2023;2(1):100015. https://doi.org/10.1016/j.enrev.2023.100015.

[43] Gillespie MI, Van Der Merwe F, Kriek RJ. Performance evaluation of a membraneless divergent electrode-flow-through (DEFT) alkaline electrolyser based on optimisation of electrolytic flow and electrode gap. J Power Sources 2015;293:228–35. https://doi.org/10.1016/j.jpowsour.2015.05.077.

[44] Hadikhani Pooria, Hashemi SMohammad H, Balestra Gioele, Zhu Lailai, Modestino Miguel A, Gallaire François, Psaltis Demetri. Inertial manipulation of bubbles in rectangular microfluidic channels. Lab Chip 2018;18(7):1035–46. https://doi.org/10.1039/C7LC01283G.

[45] Hashemi SMohammad H, Karnakov Petr, Hadikhani Pooria, Chinello Enrico, Litvinov Sergey, Moser Christophe, Koumoutsakos Petros, Psaltis Demetri. A versatile and membrane-less electrochemical reactor for the electrolysis of water and brine. Energy Environ Sci 2019;12(5):1592–604. https://doi.org/10.1039/C9EE00219G.

[46] Hadikhani Parham, Lai Daphne Teck Ching, Ong Wee-Hong, Nadimi-Shahraki Mohammad H. Automatic deep sparse multi-trial vector-based differential evolution clustering with manifold learning and incremental technique. Image Vis Comput 2023;136:104712. https://doi.org/10.1016/j.imavis.2023.104712.
[47] Martin Sergio M, Wälchli Daniel, Arampatzis Georgios, Economides Athena E, Karnakov Petr, Koumoutsakos Petros. Korali: efficient and scalable software framework for Bayesian uncertainty quantification and stochastic optimization. Comput Methods Appl Mech Eng 2022;389:114264. https://doi.org/10.1016/j.cma.2021.114264.
[48] Karnakov Petr, Litvinov Sergey, Koumoutsakos Petros. Computing foaming flows across scales: from breaking waves to microfluidics. Sci Adv 2022;8(5):eabm0590. https://doi.org/10.1126/sciadv.abm0590.
[49] Karnakov Petr, Wermelinger Fabian, Chatzimanolakis Michail, Litvinov Sergey, Koumoutsakos Petros. A high performance computing framework for multiphase, turbulent flows on structured grids. In: Proceedings of the platform for advanced scientific computing conference; 2019. https://doi.org/10.1145/3324989.3325727.
[50] Karnakov Petr, Litvinov Sergey, Koumoutsakos Petros. A hybrid particle volume-of-fluid method for curvature estimation in multiphase flows. Int J Multiphas Flow 2020;125:103209. https://doi.org/10.1016/j.ijmultiphaseflow.2020.103209.
[51] Bell John B, Colella Phillip, Glaz Harland M. A second-order projection method for the incompressible Navier-Stokes equations. J Comput Phys 1989;85(2):257–83. https://doi.org/10.1016/0021-9991(89)90151-4.
[52] Aulisa Eugenio, Manservisi Sandro, Scardovelli Ruben, Zaleski Stephane. Interface reconstruction with least-squares fit and split advection in three-dimensional Cartesian geometry. J Comput Phys 2007;225(2):2301–19. https://doi.org/10.1016/j.jcp.2007.03.015.
[53] Scardovelli Ruben, Zaleski Stephane. Analytical relations connecting linear interfaces and volume fractions in rectangular grids. J Comput Phys 2000;164(1):228–37. https://doi.org/10.1006/jcph.2000.6567.
[54] Horace E Darling. Conductivity of sulfuric acid solutions. J Chem Eng Data 1964;9(3):421–6. https://doi.org/10.1021/je60022a041.
[55] Wu Rui, Hu Zhihao, Zhang Haojing, Wang Jinqing, Qin Chaozhong, Zhou Ye. Bubbles in porous electrodes for alkaline water electrolysis. Langmuir 2023;40(1):721–33. https://doi.org/10.1021/acs.langmuir.3c02925.
[56] Lv Pengyu, Peñas Pablo, Le The Hai, Eijkel Jan, Berg Albert van den, Zhang Xuehua, Lohse Detlef. Self-propelled detachment upon coalescence of surface bubbles. Phys Rev Lett 2021;127(23):235501. https://doi.org/10.1103/PhysRevLett.127.235501.
[57] Romero-Cano MS, Martín-Rodríguez A, De las Nieves FJ. Adsorption and desorption of triton X-100 in polystyrene particles with different functionality: I. Adsorption study. J Colloid Interface Sci 2000;227(2):322–8. https://doi.org/10.1006/jcis.2000.6862.
[58] Devaraj S, Munichandraiah N. The effect of nonionic surfactant triton X-100 during electrochemical deposition of MnO2 on its capacitance properties. J Electrochem Soc 2007;154(10):A901. https://doi.org/10.1149/1.2759618.
[59] Zhao Xu, Ranaweera Ruchiranga, Luo Long. Highly efficient hydrogen evolution of platinum via tuning the interfacial dissolved-gas concentration. Chem Commun 2019;55(10):1378–81. https://doi.org/10.1039/C8CC08803A.
[60] Iwata Ryuichi, Zhang Lenan, Wilke Kyle L, Gong Shuai, He Mingfu, Gallant Betar M, Wang Evelyn N. Bubble growth and departure modes on wettable/non-wettable porous foams in alkaline water splitting. Joule 2021;5(4):887–900. https://doi.org/10.1016/j.joule.2021.02.015.
[61] Chen Yanan, Mojica Felipe, Li Guangfu, Abel Chuang Po-Ya. Experimental study and analytical modeling of an alkaline water electrolysis cell. Int J Energy Res 2017;41(14):2365–73. https://doi.org/10.1002/er.3806.
[62] Damjanovic A, Dey A, Jo'M Bockris. Kinetics of oxygen evolution and dissolution on platinum electrodes. Electrochim Acta 1966;11(7):791–814. https://doi.org/10.1016/0013-4686(66)87056-1.
[63] Kita Hideaki, Ye Shen, Gao Yunzhi. Mass transfer effect in hydrogen evolution reaction on Pt single-crystal electrodes in acid solution. J Electroanal Chem 1992;334(1–2):351–7. https://doi.org/10.1016/0022-0728(92)80583-P.
[64] Yang Gaoqiang, Yu Shule, Li Yifan, Li Kui, Ding Lei, Xie Zhiqiang, Wang Weitian, Dohrmann Yeshiemebet, Zhang Feng-Yuan. A simple convertible electrolyzer in membraneless and membrane-based modes for understanding water splitting mechanism. J Power Sources 2021;487:229353. https://doi.org/10.1016/j.jpowsour.2020.229353.
[65] Park Sunghak, Lohse Detlef, Krug Dominik, TM Koper Marc. Electrolyte design for the manipulation of gas bubble detachment during hydrogen evolution reaction. Electrochim Acta 2024;485:144084. https://doi.org/10.1016/j.electacta.2024.144084.
[66] Deng Xiaoli, Shan Yun, Meng Xiaohui, Yu Zhaoyang, Lu Xiaoxi, Ma Yunqing, Jiao Zhao, Qiu Dong, Zhang Xianren, Liu Yuwen. Direct measuring of single–heterogeneous bubble nucleation mediated by surface topology. Proc Natl Acad Sci USA 2022;119(29):e2205827119. https://doi.org/10.1073/pnas.2205827119.
[67] Giribabu K, Ghosh P. Adsorption of nonionic surfactants at fluid–fluid interfaces: importance in the coalescence of bubbles and drops. Chem Eng Sci 2007;62(11):3057–67. https://doi.org/10.1016/j.ces.2007.03.002.
[68] Moradi Nafchi F, Afshari E, Baniasadi E. Anion exchange membrane water electrolysis: numerical modeling and electrochemical performance analysis. Int J Hydrogen Energy 2024;52:306–21. https://doi.org/10.1016/j.ijhydene.2023.05.173.